



Transport and eruption of mantle xenoliths creates a lagging problem

James K. Russell ¹ & Thomas J. Jones ²✉

Mantle-derived xenoliths entrained by low viscosity magmas indicate transport through great thicknesses of orogenic ($\lesssim 50$ – 80 km) and cratonic ($\lesssim 20$ km) mantle lithosphere. The size and density of xenoliths dictate that, relative to the ascending magma, they continuously settle during transport. This creates a lag time between when the initial sampling magma reaches the Earth's surface and the arrival of the xenoliths. The magnitude of this lag time depends on xenolith properties, sampling depth and the magma ascent velocity. Here, using settling calculations, we develop this lag time concept and show how eruption durations and volumes can impact the distribution, abundance, and properties (e.g., sample depths, size) of xenoliths. Lag times can account for heterogeneous xenolith distributions within volcanic deposits, the potential biased sampling of the mantle lithosphere, and can constrain minimum eruption volumes required to transport and erupt the deepest sourced xenoliths such as those producing diamondiferous kimberlites.

¹Earth, Ocean & Atmospheric Sciences, The University of British Columbia, Vancouver, BC, Canada. ²Lancaster Environment Centre, Lancaster University, Lancaster LA1 4YQ, UK. ✉email: thomas.jones@lancaster.ac.uk

Crustal and mantle xenoliths—foreign rock fragments incorporated into magmas—are a common occurrence within volcanic deposits spanning a wide range of magma compositions and eruption styles. Crustal-derived xenoliths are used to establish the age and origins of the crustal lithosphere^{1–3}, to create stratigraphic cross-sections for the mid-to-lower crust⁴, to constrain its thermal history and state, and to document the physical-chemical conditions within trans-crustal magmatic systems^{5–7}. Within physical volcanology, crustal xenoliths inform on syn-eruptive conduit erosion and fragmentation depths during explosive eruptions^{8–10}.

Xenoliths of the mantle lithosphere, the focus here, are found in a wide variety of alkaline and related magmatic deposits, such as nephelinites, basanites, lamprophyres, and kimberlite. Much of our knowledge of the mineralogical and geochemical composition, thermal state, structural properties, age, and origins of the subcontinental mantle lithosphere derives from petrological^{11–14}, geochemical^{15–19}, and structural^{20–23} studies of peridotite, pyroxenite, and eclogite xenoliths recovered from volcanic and magmatic deposits. Thus, direct studies of the mantle lithosphere rely on successful sampling, entrainment, and eruption of these xenoliths by mantle-derived melts.

Mantle xenoliths also constrain the average rates of the ascent of their host magmas. For example, xenoliths are commonly thermally equilibrated with the host magma during transport but are not (fully) chemically equilibrated. Their mineralogy and mineral compositions still record original mantle pressure-temperature conditions²⁴, implying that there is insufficient time during transport for the slower, chemical equilibrium to be achieved^{19,25}. Many other indicators of chemical disequilibrium have been exploited to constrain magma ascent rates^{26–28}, with a full review provided by Rutherford²⁸. High-temperature experiments have been used to quantify the rates of specific mineral-melt reactions thereby constraining minimum and maximum ascent rates. Examples include decompression-driven degassing and groundmass crystallization experiments, mineral (phenocryst or xenocryst) reaction or dissolution experiments^{29,30}, and melt-crystal diffusion experiments³¹ (e.g., H diffusion in olivine^{32–34}; Ar diffusion in phlogopite³⁵).

Lastly, magma ascent rates are commonly estimated using the simple premise that the magma must rise faster than the xenolith can settle^{27,36,37}. Despite the limiting implicit assumptions, these

calculations indicate that, during transport, the dense mantle cargo is continually settling relative to the less dense, low-viscosity magma. This implies that xenoliths can separate from the host magma wherein a substantial lag time develops between the eruption of the original magma that sampled the mantle and eruption of the associated, yet lagging, xenolithic cargo. Here, we illustrate the feasibility for, and extent of, this decoupling between magma and xenoliths and explore the implications for heterogeneous and biased distributions of mantle material within volcanic deposits, as well as, the transport of diamondiferous mantle cargo.

Results and discussion

Xenolith sampling and properties. Mantle xenoliths are generated through brittle deformation of lithospheric wall rocks, especially where magmas exsolve CO₂–H₂O-rich fluids. Stresses imposed at the crack tip, at the head of the buoyant magma (Fig. 1a), exceed the tensile strength of the wall rocks causing damage and failure^{27,37–41}. Subsequent propagation of the dyke through the damaged mantle lithosphere samples and entrains xenoliths⁴². Continued and sequential dyke propagation, driven by increasing buoyancy, promotes magma ascent and repeated sampling of the lithosphere.

Most mantle xenolith-bearing magmas (e.g., nephelinite, basanite, kimberlite, lamprophyre) have low viscosities on the order of 1 to 100 Pa s, erupt at high temperatures⁴³ (~1050–1350 °C) with low phenocryst contents, and have vesicle-free densities (ρ_m) of ~2700 kg m⁻³ (e.g., basanite, nephelinite) to ~3000 kg m⁻³ (e.g., kimberlite)^{27,44,45}. Despite traveling substantial distances through the mantle lithosphere, these magmas can erupt with high loads ($\lesssim 25$ vol. %) of large, dense (~3250 kg m⁻³) mantle cargo (Fig. 1b). The mantle xenoliths found in alkaline volcanic rocks are commonly 5–25 cm in diameter (Fig. 1c), but maximum sizes reported^{25,46–48} reach 25–80 cm. Once entrained, there is a large density contrast ($\Delta\rho \sim 250$ –550 kg m⁻³) between the xenoliths and the magma which promotes xenolith settling. Importantly, the low viscosity of alkaline magmas at near-liquidus temperatures means that substantial settling can occur on timescales coincident with transport and eruption.

Quantitative field data on the abundance, size distribution, and stratigraphic position (i.e., relative eruption timing) of mantle xenoliths within volcanic deposits are sparse. However, there is



Fig. 1 Sampling and entrainment of mantle-derived xenoliths. **a** Schematic representation of the origins of mantle-derived xenoliths. The fragmented mantle is entrained by magma with a rise velocity (V_m). Once entrained, xenoliths sink continuously (V_T) depending on the density difference between xenolith and magma ($\Delta\rho = \rho_x - \rho_m$) and on the xenolith diameter, **b** Outcrop-scale field photograph of abundant peridotitic mantle xenoliths within a 1–7 m wide basanite dyke exposed at Mount Preston, British Columbia, Canada⁸⁸. **c** Deposit-scale field photograph showing xenolith size (d –5 to 40 cm), shape and near clast-supported distribution of mantle xenoliths within the same basanite dyke. The authors have obtained consent for publication of the images showing individuals.

abundant qualitative, descriptive evidence for uneven xenolith abundances within deposits, indicating some degree of decoupling between xenoliths and the host magma. Examples of eruptions producing variably xenolith-enriched deposits include the 1730–1736 eruption of alkaline lavas from Lanzarote, Canary Islands⁴⁹; the 1800 Hualalai lavas, Hawaii^{50,51}; the monogenetic Bakony–Balaton Highland Volcanic Field, Hungary⁵²; the Pello Hill scoria cone, Tanzania⁵³; and the Homestead kimberlite, Montana²⁵. Furthermore, in several instances, mantle xenoliths were reported as erupting late, relative to the onset of the eruption^{54,55}, consistent with the concept of a lag time.

Xenolith-settling basics. Stokes Law is a constraint on the minimum magma ascent velocities required for successful entrainment and transport of xenoliths³⁷. It provides an idealized estimate of the terminal settling velocities (V_T) of dense solids (xenoliths) in magmas as a function of magma viscosity (η), xenolith radius (r) and the density contrast between xenolith and magma ($\Delta\rho = \rho_x - \rho_m$):

$$V_T = \frac{(2g\Delta\rho r^2)}{9\eta}. \quad (1)$$

The relationship between magma viscosity and Stokes settling velocity (Eq. (1)) for a range of xenolith sizes ($r = d/2$) is shown in Fig. 2a. The terminal settling velocity estimates are valid for spherical particles settling within the laminar flow regime at particle Reynolds numbers (Re_p) less than or equal to unity:

$$Re_p \leq 1 = \frac{V_T \rho_m d}{\eta}. \quad (2)$$

The Stokes settling velocity (Eq. (1)) constrained to the condition $Re_p \sim 1$ (Eq. (2)) defines a critical viscosity value (η_c) as:

$$\eta_c = \sqrt{\frac{4g\Delta\rho\rho_m r^3}{9}}. \quad (3)$$

Substitution of Eq. (3) into the Stokes equation yields a critical settling velocity (V_{Tc}), consistent with $Re_p \sim 1$, described by:

$$V_{Tc} = \left(\frac{g\Delta\rho r}{9\rho_m}\right)^{0.5}. \quad (4)$$

At lower viscosity and higher settling rates, values of Re_p exceed 1 (Fig. 2a; dashed lines). For example, larger xenoliths have higher settling rates and to meet the condition $Re_p < 1$ would require transport in a higher viscosity magma (Fig. 2a). This limiting condition ($Re_p > 1$), however, does not negate the high settling rates of xenoliths in low-viscosity magmas. It simply means that xenoliths are settling at a rate that is not necessarily the exact velocity predicted by Stokes's law.

Xenoliths—coupled or not? Previous studies have invoked a yield stress (e.g., Bingham rheology) to enhance xenolith-magma coupling and explain the ubiquitous and successful transport of xenoliths^{27,28,36,56}. Sparks et al.³⁶ argued that yield strengths of 10–1000 Pa, corresponding to crystal contents >25 vol. %, would allow for xenoliths up to 30 cm in diameter to couple with the ascending magma. Similarly, Spera²⁷ suggested a yield strength of 100 Pa (~25 vol. % crystals) could couple xenoliths up to ~5 cm in diameter to the magma. However, to cause a 50% reduction in settling velocity of, for example, a 30 cm xenolith would require a yield strength of 500–1000 Pa achieved only by a substantially higher magma crystallinity²⁷.

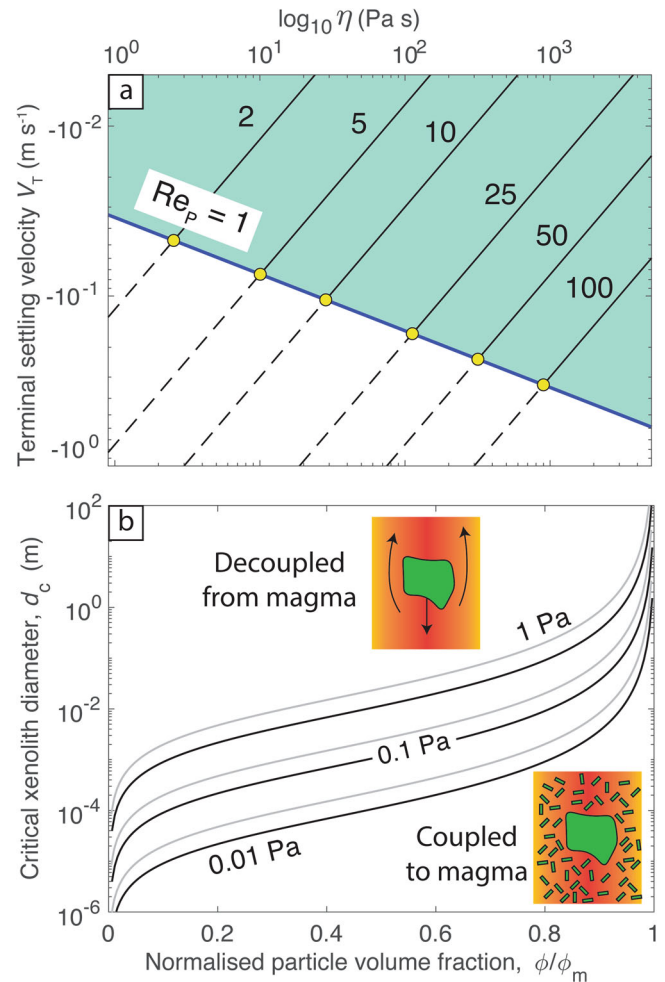


Fig. 2 Stokes terminal settling velocities (Eq. 1) of mantle xenoliths.

a Xenolith-settling velocities (–ve) calculated as a function of the magma viscosity (η ; Pa s) and xenolith diameter (d ; 2–100 cm). Solid lines indicate velocities where $Re_p < 1$; dashed lines indicate $Re_p > 1$. The thick blue line marks the $Re_p \sim 1$ constraint (Eq. (2)). **b** The critical xenolith diameter, d_c , at which xenoliths with density $\rho_x = 3250 \text{ kg m}^{-3}$ overcome magma yield stress and can settle. Values of d_c calculated as a function of the crystal content, where ϕ is the crystal volume fraction and ϕ_m is the maximum packing fraction. Three different fitting parameters of τ^* (i.e., 0.01, 0.1, and 1 Pa) are shown for magma density values of 2700 kg m^{-3} (black lines) and 3000 kg m^{-3} (gray lines). These values cover the full range of particle sizes and shapes typical of natural systems.

Coupling between the xenolith and magma can be quantitatively evaluated using the Yield number^{57,58}:

$$Y = \frac{3\tau_y}{gd(\rho_x - \rho_m)} \quad (5)$$

where τ_y is the yield stress and g is the gravitational acceleration. For a spherical particle, above a critical Y of 0.145 there is no motion—the xenolith cannot settle, and it is held in place by the yield strength of the host magma^{57–60}. Yield stresses are not observed for crystal volume fractions (ϕ) significantly below the maximum packing fraction, ϕ_m . It is only where $\phi/\phi_m \geq 0.8$ that appreciable yield stresses develop for all crystal sizes⁶¹. Heymann et al.⁶² have shown that yield stresses increase with increasing

particle volume fraction by the following relationship:

$$\tau_y = \tau^* \left(\left(1 - \frac{\phi}{\phi_m} \right)^{-2} - 1 \right) \quad (6)$$

where τ^* is a fitting parameter related to the size and shape of the crystals. Although no functional form exists relating crystal size to τ^* , generally larger crystals have a lower τ^* and thus provide a lower yield strength. For reasonable^{61,62} and cautious values of τ^* ranging from 0.01 to 1 Pa, corresponding to approximate crystal diameters ranging from 100 to 1 μm , respectively, we find that the critical xenolith diameter (d_c) required to overcome the yield stress is very small (Fig. 2b). Even small xenoliths <10 cm can readily decouple from the host magma. It is only at unrealistic particle volume fractions $\phi/\phi_m \geq 0.8$ that xenolith sizes <20 cm can be transported without appreciable settling. This is further compounded by the fact that most alkaline magmas carrying large volumes of mantle xenoliths have relatively low (micro-) phenocryst contents indicating ascent at near-liquidus temperatures, thereby, precluding extensive groundmass crystallization. Whilst extensive cooling and crystallization could provide the required yield strength for xenolith coupling, continued magma ascent and eruption would become implausible²⁷. In addition, as argued by Spera²⁷, there is no field-based correlation between

crystal contents (i.e., yield stress) of xenolith-bearing magmas and xenolith abundance.

Our analysis suggests that mantle xenoliths are unlikely to be coupled to their host magmas by a yield stress during ascent through the lithosphere^{27,36}. Thus, we contend that xenoliths are variably decoupled from the magma and are subject to settling for the duration of ascent. A large, appreciable time difference—a lag time—must develop between the surface eruption of xenoliths and the magmas that originally sampled them.

Xenolith lag times. Dense mantle-derived xenoliths reach the surface; this implies that host magmas ascend from the sampling depths (X_s) at velocities (V_m) faster than the xenoliths are sinking (V_T). For example, a 25-cm diameter peridotite xenolith sampled and entrained by an alkaline magma ($\eta \sim 10 \text{ Pa s}$; $\Delta\rho \sim 550 \text{ kg m}^{-3}$) at 50-km depth (X_s) will potentially settle through the magma with a velocity of $\sim -2 \text{ m s}^{-1}$ (V_T ; Fig. 3a). A kimberlite magma ascending at 4 m s^{-1} (V_m) can drag the xenolith upwards at a net rise rate ($V_x = V_m + V_T$) of $\sim 2 \text{ m s}^{-1}$. The differential velocity between the magma and the xenolith results in a lag time that increases with transport distance. A xenolith sampled at 50-km depth arrives at the Earth’s surface 3 h after the eruption of the magma that originally entrained the

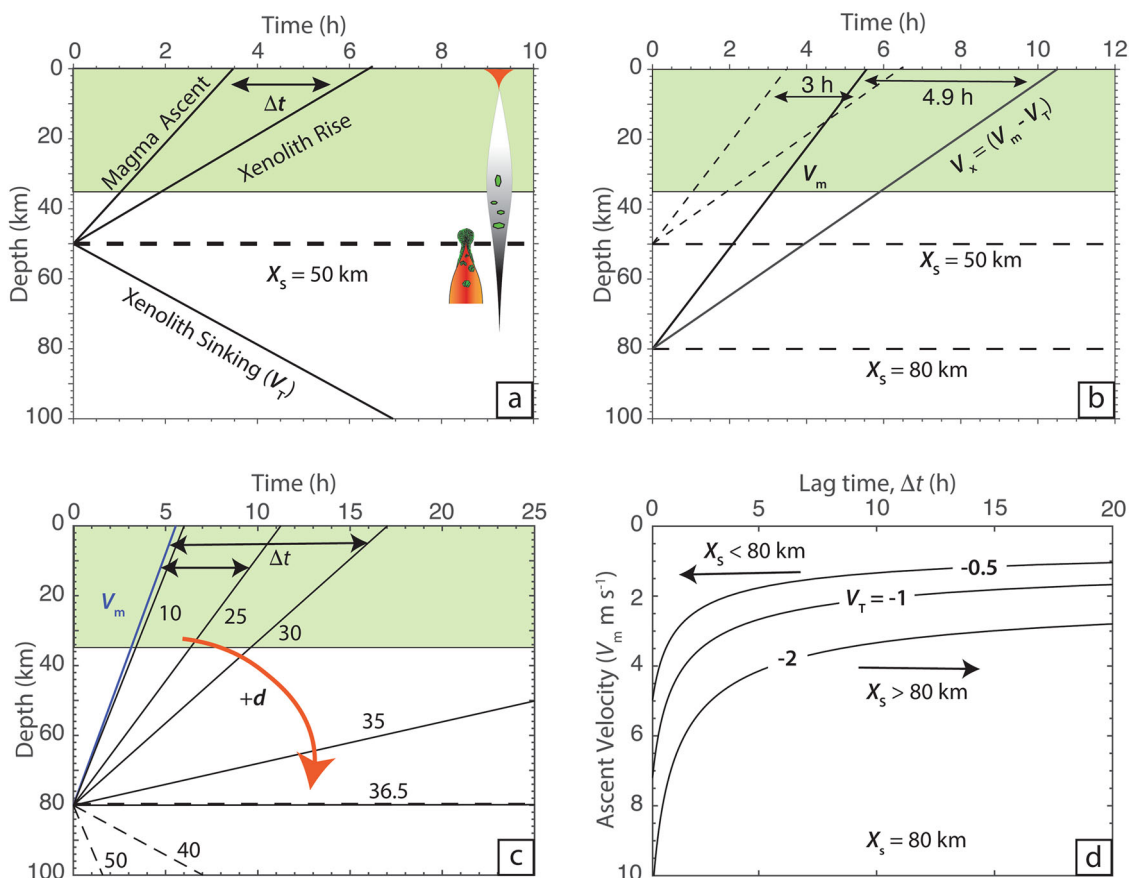


Fig. 3 Controls on xenolith transport times and lag times (Δt). **a** Lag time calculated for a 25 cm diameter xenolith sampled and entrained at mantle depth of 50 km (X_s). Magma ascends at (V_m) 4 m s^{-1} and xenolith has V_T of -2 m s^{-1} resulting in a xenolith rise velocity ($V_x = V_m - V_T$) of 2 m s^{-1} . **b** Comparison of transport and lag times for same-sized xenolith ($d = 25 \text{ cm}$) entrained at different depths ($X_s = 50$ and 80 km). **c** Model transport times and lag times (Δt) of xenoliths labeled for different diameters (cm) sampled at the same depth ($X_s = 80 \text{ km}$) within a magma ascending at 4 m s^{-1} (blue line). Xenoliths greater than $d = 36.5 \text{ cm}$ are sinking continuously relative to their sample site. **d** Calculated lag times for xenoliths settling at different rates ($V_T = -0.5, -1, \text{ and } -2 \text{ m s}^{-1}$) as a function of magma ascent rate (V_m) for a source depth (X_s) of 80 km . Arrows indicate the relative effects of source depth on lag time. Lag times increase with lower magma ascent rates and higher rates of xenolith settling. Curves shown for different xenolith-settling rates approach infinity as V_m approaches V_T .

xenolith (Fig. 3a). For a deeper sampling depth of 80 km, the lag time increases to ~5 h (Fig. 3b).

The lag time (Δt) can be directly expressed in terms of source depth (X_s) and the rise velocities of, both, the magma (V_m) and xenolith (V_x):

$$\Delta t = \frac{V_T X_s}{V_m(V_m + V_T)} = X_s \left[\frac{1}{V_m} - \frac{1}{V_x} \right], \quad (7)$$

making the velocity differentials independent of Stokes Law and its assumptions. In general, the deeper sourced mantle xenoliths will have the greatest lag times, as well as the greatest transport durations (Eq. (7); Fig. 3b). Shallow sampled mantle xenoliths will have shorter residence times and have shorter or no appreciable lag times. Crustal xenoliths, having lower density, are likely to be better coupled to the magma and erupted continuously with the original magma⁶³.

The magma-xenolith differential velocities are mainly a function of the mantle xenolith size (Fig. 3c). For a sampling depth (X_s) of 80 km and V_m of 4 m s⁻¹, smaller ($d \leq 10$ cm) xenoliths have lag times <1 h. However, increasing the xenolith size to $d = 25$ cm generates lag times that imply a minimum of ~5 h of continuous eruption preceding the xenoliths reaching the surface. Larger xenoliths having $d \sim 30$ cm generate lag times >10 h. The settling velocities for xenoliths $> d = 36.5$ cm exceed the magma ascent rate of 4 m s⁻¹ and are not easily carried to the surface (Fig. 3c).

Increasing magma ascent rates can drastically reduce lag times for xenoliths of similar size and density sampled at the same depth (Fig. 3d). For a fixed xenolith-settling velocity of -2 m s⁻¹, the lag time for xenoliths sampled at 80 km depth decreases from ~7 h to ~2 h for magma ascent velocities (V_m) of 4 vs. 6 m s⁻¹, respectively. For the same ascent rates, smaller xenoliths with lower settling velocities (i.e., -1 to -0.5 m s⁻¹) will have lag times between 2 h and minutes. As values of V_m approach $-V_T$, lag times approach infinity (Fig. 3d).

A direct consequence of the lag time concept is that most xenoliths sampled at depths of X_s are inherited and erupted by later magmas that were situated deeper (D_m) at the time of sampling:

$$D_m = \frac{V_m X_s}{V_m + V_T} = \frac{V_m X_s}{V_x}. \quad (8)$$

The pairing between magma and xenoliths at the surface is dependent on their relative rise velocities and the xenolith sampling depth. This value of D_m serves as a proxy for the minimum supply of magma passing through the system and required to drag the lagging xenolith to the eruption point. This also emphasizes the petrological and geochemical disconnection between mantle xenoliths and the nature and composition of the magma that carries them.

Modification of cargo. Extended residence time, due to lagging, within the host magma promotes a variety of physical and chemical processes that modify the mantle cargo. Rapid upwards flow facilitates mechanical abrasion of xenoliths by particle-particle interactions^{9,42,64–69} promoting resizing, reshaping (i.e., rounding), and resurfacing (i.e., roughness) of the mantle material.

Prolonged residence times within the host magma can also promote (partial) chemical re-equilibration of mantle minerals driven by changes in pressure-temperature conditions or by chemical (e.g., Fe, Mg, H) exchanges with the transporting melt¹⁹. Potentially, finer-grained, deeply sourced, large xenoliths have the greatest potential for partial thermal-chemical re-equilibration (i.e., porphyroclastic or sheared peridotites). Furthermore, a

by-product of abrasive milling, is the concomitant production of fine chips of mantle minerals^{66,68} which are highly susceptible to magmatic assimilation during transport. Lastly, large, uncoupled xenoliths (i.e., $V_m \neq V_x$) are susceptible to ablation-driven assimilation⁷⁰ which can accelerate dissolution processes driven by chemical disequilibrium between the xenolith mineral assemblage and the magma⁷¹.

Sorting, mixing and biased sampling. Sorting of xenolithic material by size alone during magma transport is an inefficient process and leads to xenolith clusters, each representing a single sampling event during episodic dyke propagation. The magma rises faster than most xenoliths, allowing stratification to be maintained, wherein shallower sampled xenoliths lead the way ahead of clusters of xenoliths from the earlier, deeper sampling events. This can promote highly disparate distributions within intrusive deposits (e.g., dykes), where deposits contain only crustal xenoliths or only mantle xenoliths or both (cf. Fig. 1b). Consequently, geothermobarometric studies of xenoliths within individual volcanic deposits may vary greatly depending on which phases of eruption the deposits represent. Volcanic eruption processes, particularly explosive processes, on the other hand, provide a means of dispersing and mixing xenolith populations.

During transport, magma properties will not be constant but evolve from the deep mantle, through the lithosphere, to the point of eruption^{24,28,43,72}. Solid particles, such as xenoliths and xenocrysts in silicate magmas can enhance nucleation of H₂O/CO₂ bubbles^{40,73}. Experiments using carbonated liquids and solids demonstrate the importance of rough surfaces for causing rapid, heterogeneous bubble nucleation⁷⁴. Longer xenolith transport times support abrasive processes^{66–68} which will roughen xenolith surfaces, potentially facilitating vesiculation^{40,75}.

Rapidly increasing magma vesicularity can promote further decoupling between the magma and xenolith and increase xenolith lag times in two ways. First, the transition to a high-vesicularity magma will decrease the bulk magma density and, under the high eruption velocity (i.e., high shear-rate) conditions characteristic of these magmas^{26,41,45,66,76}, will decrease the bulk magma viscosity. This will increase xenolith settling and lag times. Second, for these low-viscosity magmas bubble exsolution will be followed by efficient bubble coalescence, promoting separated fluid flow⁷⁷. This can lead to a stratified magma column⁴² featuring a gas-dominated head followed by bubble-rich magma, and a relatively gas-poor, xenolith-rich tail. This stratification of the magma column results in an energetic explosive eruption onset (i.e., the arrival of a xenolith-absent gas-rich head) followed by a continuing decrease in intensity and concludes with an effusive eruption. These eruptive processes have the capacity to create highly heterogeneous distributions of xenoliths, wherein, different phases (i.e., early versus late) have no xenoliths, or only small xenoliths, or host most of the larger xenoliths. We might expect, for example, explosive and effusive eruption products to have vastly different xenolith populations.

Making (diamondiferous) kimberlite. The transport of mantle xenoliths by kimberlite magmas is of particular interest because they have ultra-deep¹⁸ mantle sources (200–600 km) and erupt after transiting 190–220 km of cratonic mantle lithosphere^{12,78–80}. Despite traveling such large distances, they erupt xenoliths sampled from even the deepest cratonic mantle⁸¹ (i.e., >150 km), including xenoliths from within the lithospheric diamond stability field or diamond window (depths \geq 120–130 km; Fig. 4a).

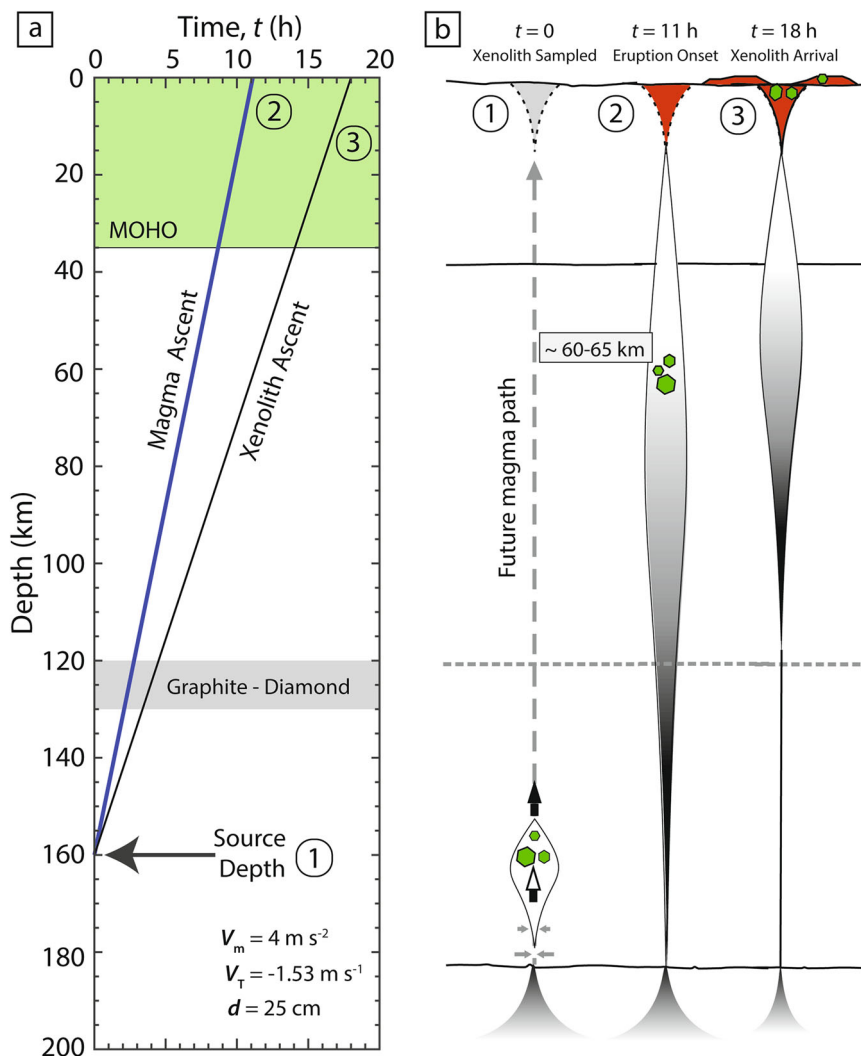


Fig. 4 Schematic illustration of transport of mantle xenoliths by kimberlite magmas ($\rho_m = 2800 \text{ kg m}^{-3}$; $\eta = 10 \text{ Pa s}$). **a** The xenoliths shown in this figure are sampled and entrained at depths within the diamond stability field ($>120\text{--}130 \text{ km}$). The lag time ($\Delta t \sim 7 \text{ h}$) developed for an initial magma with an ascent velocity of 4 m s^{-1} and a xenolith ($d = 25 \text{ cm}$) sampled at 160 km ($V_T \sim -1.5 \text{ m s}^{-1}$). Values of Δt will be less for smaller xenoliths and much greater for larger xenoliths (cf. Fig. 3c). **b** Illustrations corresponding to specific points on the graph: (1) time of sampling ($t = 0$); (2) the onset of eruption ($t = 11 \text{ h}$), and (3) the surface arrival of those xenoliths carried by later magma ($t = 18 \text{ h}$).

Lag times are especially important for kimberlites because the deeply sourced, potentially diamond-bearing xenoliths can erupt hours after eruption onset. If eruption durations are short, erupted magma volumes are low, or ascent stalls, xenoliths are at risk of being left within the subsurface. Furthermore, the earliest eruptions could be completely devoid of xenoliths or, at least, devoid of those from within the diamond stability field (Fig. 4a, b). Xenolith size is also an important factor because larger xenoliths provide greater preservation of diamond (i.e., limited dissolution, graphitization, decarbonation). Indeed, although kimberlites originate from depths below the diamond window, not all kimberlite bodies have economic grades of diamond^{82,83}. Eruption duration, therefore, may be an important factor contributing to the presence and distribution of diamonds within kimberlites. For a kimberlite magma with an average ascent rate⁴⁵ of 4 m s^{-1} , there are $\sim 11 \text{ h}$ of transit time once it leaves a mantle depth of $\sim 160 \text{ km}$ (Fig. 4; Points 1–2). Average sized xenoliths ($d \sim 25 \text{ cm}$) sampled at 160 km would have lag times of $\sim 7 \text{ h}$ and total transit times of 18 h before eruption. If magma ascends at 4 m s^{-1} within a 1 m wide dyke having a 1 km strike length, then at the onset of eruption ($t = 11 \text{ h}$; Fig. 4; Point

2) $158 \times 10^6 \text{ m}^3$ of magma has passed the original depth of xenolith sampling and has carried the xenoliths to within $60\text{--}65 \text{ km}$ of the Earth's surface. Later, when these xenoliths are being erupted ($t = 18 \text{ h}$; Fig. 4; Points 2–3) the minimum volume of erupted material is $100 \times 10^6 \text{ m}^3$ and more than $250 \times 10^6 \text{ m}^3$ of magma has passed through the diamond window. Continued eruption from this time onward enhances the potential for producing diamond-bearing kimberlite deposits.

This minimum erupted volume ($100 \times 10^6 \text{ m}^3$) is ~ 25 times larger than the volume of the Quaternary Igwisi Hills kimberlites, Tanzania ($3.5 \times 10^6 \text{ m}^3$) which are devoid of diamond and large xenoliths. The Igwisi Hills kimberlites only contain abundant micro-xenoliths ($d \lesssim 1 \text{ cm}$) of mantle material and olivine xenocrysts^{84,85}. Shaikh et al.⁸⁰ suggest that these micro-xenoliths are from relatively shallow sources ($100\text{--}145 \text{ km}$), indicating that the deepest-seated and largest xenoliths failed to make it to the eruption point. This supports the idea that the eruption at Igwisi Hills was too short in duration, erupting too small a volume of magma, to sustain the ascent of the larger, deeper-seated diamondiferous mantle cargo. Those materials were able to lag-out before eruption. In contrast, the minimum

Table 1 An example calculation.

Property	Symbol	Value	Model calculation	
Density (kg m ⁻³ ; ρ)	ρ_x	3250	V_T (m s ⁻¹)	−0.94
	ρ_m	2700		
Viscosity (Pa s; η)	η	20	Re_p	31.6
			Δt (h) $X_s = 60$ km	1.27
Diameter (m)	d	25	Δt (h) $X_s = 150$ km	3.18
Magma rise rate (m s ⁻¹)	V_m	4		

Physical properties assigned to an average alkaline mafic magma (subscript m) and mantle xenoliths (subscript x) for lag time (Δt) calculations. For the example in this table, we use a magma rise rate (V_m) of 4 m s⁻¹, a xenolith having diameter (d) of 25 cm, and source depths (X_s) of 60 and 150 km. Also calculated are values for the xenolith terminal settling velocity (V_T) and the particle Reynolds number (Re_p).

preserved volumes of many of the older, partially eroded, diamondiferous kimberlite pipes comprising the Lac du Gras kimberlite cluster in Canada⁸⁶ (e.g., A418 pipe) are equal to, or greater than, 100×10^6 m³. Many diamondiferous pipes in South Africa⁸⁷ are even larger (10^{7-8} m³). Furthermore, Tappe et al.⁸² showed that for any major kimberlite cluster on the Kalahari craton the highest-grade kimberlite pipe is typically the largest. This can be explained by our lag time concept—for kimberlites to be diamondiferous they must erupt large magma volumes, for long enough, to allow lagging mantle xenoliths originating from the lithospheric diamond window to reach the surface.

Methods

Calculation of xenolith-settling velocity. We use Stokes Law for the terminal settling velocity (V_T) of particles in a viscous fluid as a proxy for the rate at which a mantle xenolith could settle through the host magma: $V_T = 2g\Delta\rho r^2/(9\eta)$. The settling velocity depends on the density contrast between xenolith and magma ($\Delta\rho$), the size (radius) of the xenolith (r), and magma viscosity (η). We use average properties for the magma and a range of xenolith sizes based on observations published in the literature. An example calculation is presented in Table 1.

The calculated values of V_T are then compared to a range of assumed magma ascent velocities. This is used to find the differential rise rate between the magma and the entrained xenoliths. We model the lag time (Δt) that results from the differences in rise rates as $\Delta t = X_s (1/V_m - 1/V_x)$. The lag time between the eruption of the magma and the xenoliths it sampled is modeled as a function of source depth and magma rise velocity. If the differential velocity between the xenolith and magma is known or established independently, we can calculate lag times that are not explicitly dependent on Stokes Law. The general idea and consequences of a lag time are explored within this manuscript.

Data availability

The data generated or analyzed in this study are provided in the main article and can be accessed via Zenodo (<https://doi.org/10.5281/zenodo.7904005>).

Code availability

The xenolith settling and lag time calculations were performed using MATLAB. Our code can be accessed via Github/Zenodo (<https://doi.org/10.5281/zenodo.7818407>).

Received: 11 January 2023; Accepted: 9 May 2023;

Published online: 24 May 2023

References

- Leeman, W. P., Menzies, M. A., Matty, D. J. & Embree, G. F. Strontium, neodymium and lead isotopic compositions of deep crustal xenoliths from the Snake River Plain: evidence for Archean basement. *Earth Planet. Sci. Lett.* **75**, 354–368 (1985).
- Rudnick, R. L. Xenoliths—samples of the lower continental crust. *Cont. Low. crust* **23**, 269–316 (1992).
- Condie, K. C. Mafic crustal xenoliths and the origin of the lower continental crust. *Lithos* **46**, 95–101 (1999).
- Ghent, E. D., Edwards, B. R., Russell, J. K. & Mortensen, J. Granulite facies xenoliths from Prindle volcano, Alaska: implications for the northern Cordilleran crustal lithosphere. *Lithos* **101**, 344–358 (2008).
- Melekhova, E., Blundy, J., Martin, R., Arculus, R. & Pichavant, M. Petrological and experimental evidence for differentiation of water-rich magmas beneath St. Kitts, Lesser Antilles. *Contrib. to Mineral. Petrol.* **172**, 1–32 (2017).
- Hacker, B. R. et al. Hot and dry deep crustal xenoliths from Tibet. *Science* **287**, 2463–2466 (2000).
- Rudnick, R. L. & Fountain, D. M. Nature and composition of the continental crust: a lower crustal perspective. *Rev. Geophys.* **33**, 267–309 (1995).
- Doubik, P. & Hill, B. E. Magmatic and hydromagmatic conduit development during the 1975 Tolbachik eruption, Kamchatka, with implications for hazards assessment at Yucca Mountain, NV. *J. Volcanol. Geotherm. Res.* **91**, 43–64 (1999).
- Campbell, M. E., Russell, J. K. & Porritt, L. A. Thermomechanical milling of accessory lithics in volcanic conduits. *Earth Planet. Sci. Lett.* **377**, 276–286 (2013).
- Eychenne, J., Le Pennec, J.-L., Ramon, P. & Yepes, H. Dynamics of explosive paroxysms at open-vent andesitic systems: high-resolution mass distribution analyses of the 2006 Tungurahua fall deposit (Ecuador). *Earth Planet. Sci. Lett.* **361**, 343–355 (2013).
- Kukkonen, I. T. & Peltonen, P. Xenolith-controlled geotherm for the central Fennoscandian Shield: implications for lithosphere-asthenosphere relations. *Tectonophysics* **304**, 301–315 (1999).
- Russell, J. K. & Kopylova, M. G. A steady state conductive geotherm for the north central Slave, Canada: inversion of petrological data from the Jericho Kimberlite pipe. *J. Geophys. Res. Solid Earth* **104**, 7089–7101 (1999).
- Harder, M. & Russell, J. K. Thermal state of the upper mantle beneath the Northern Cordilleran Volcanic Province (NCVP), British Columbia, Canada. *Lithos* **87**, 1–22 (2006).
- Edwards, B. R. & Russell, J. K. Distribution, nature, and origin of Neogene-Quaternary magmatism in the northern Cordilleran volcanic province, Canada. *Geol. Soc. Am. Bull.* **112**, 1280–1295 (2000).
- Peslier, A. H., Reisberg, L., Ludden, J. & Francis, D. Os isotopic systematics in mantle xenoliths; age constraints on the Canadian Cordillera lithosphere. *Chem. Geol.* **166**, 85–101 (2000).
- O'Reilly, S. Y. & Griffin, W. L. The continental lithosphere-asthenosphere boundary: can we sample it? *Lithos* **120**, 1–13 (2010).
- Pearson, D. G. & Wittig, N. The formation and evolution of cratonic mantle lithosphere – evidence from mantle xenoliths. In *Treatise on Geochemistry* 2nd edn. (Eds Holland, H. D. & Turekian, K. K.) 255–292 (Elsevier, 2014).
- Pearson, D. G., Woodhead, J. & Janney, P. E. Kimberlites as geochemical probes of Earth's mantle. *Elem. An Int. Mag. Mineral. Geochemistry, Petrol* **15**, 387–392 (2019).
- Canil, D., Russell, J. K. & Fode, D. A test of models for recent lithosphere founding or replacement in the Canadian Cordillera using peridotite xenolith geothermometry. *Lithos* **398**, 106329 (2021).
- Mercier, J. C. C. & Nicolas, A. Textures and fabrics of upper-mantle peridotites as illustrated by xenoliths from basalts. *J. Petrol.* **16**, 454–487 (1975).
- Lallemant, H. G. A., Mercier, J. C. C., Carter, N. L. & Ross, J. V. Rheology of the upper mantle: inferences from peridotite xenoliths. *Tectonophysics* **70**, 85–113 (1980).
- Ross, J. V. The nature and rheology of the Cordilleran upper mantle of British Columbia: inferences from peridotite xenoliths. *Tectonophysics* **100**, 321–357 (1983).
- Kennedy, L. A., Russell, J. K. & Kopylova, M. G. Mantle shear zones revisited: the connection between the cratons and mantle dynamics. *Geology* **30**, 419–422 (2002).

24. Mitchell, R. H., Carswell, D. A. & Clarke, D. B. Geological implications and validity of calculated equilibration conditions for ultramafic xenoliths from the Pipe 200 kimberlite, northern Lesotho. *Contrib. to Mineral. Petrol.* **72**, 205–217 (1980).
25. Hearn, B. C. The Homestead kimberlite, central Montana, USA: mineralogy, xenocrysts, and upper-mantle xenoliths. *Lithos* **77**, 473–491 (2004).
26. Egger, D. H. Kimberlites: how do they form. *Kimberlites Relat. rocks* **1**, 489–504 (1989).
27. Spera, F. J. Carbon dioxide in petrogenesis III: role of volatiles in the ascent of alkaline magma with special reference to xenolith-bearing mafic lavas. *Contrib. to Mineral. Petrol.* **88**, 217–232 (1984).
28. Rutherford, M. J. Magma ascent rates. *Rev. Mineral. Geochemistry* **69**, 241–271 (2008).
29. Klügel, A., Hansteen, T. H. & Schmincke, H.-U. Rates of magma ascent and depths of magma reservoirs beneath La Palma (Canary Islands). *Terra Nov.* **9**, 117–121 (1997).
30. Canil, D. & Fedortchouk, Y. Garnet dissolution and the emplacement of kimberlites. *Earth Planet. Sci. Lett.* **167**, 227–237 (1999).
31. Mackwell, S. J. & Kohlstedt, D. L. Diffusion of hydrogen in olivine: implications for water in the mantle. *J. Geophys. Res. Solid Earth* **95**, 5079–5088 (1990).
32. Peslier, A. H., Woodland, A. B. & Wolff, J. A. Fast kimberlite ascent rates estimated from hydrogen diffusion profiles in xenolithic mantle olivines from southern Africa. *Geochim. Cosmochim. Acta* **72**, 2711–2722 (2008).
33. Peslier, A. H. & Luhr, J. F. Hydrogen loss from olivines in mantle xenoliths from Simcoe (USA) and Mexico: Mafic alkalic magma ascent rates and water budget of the sub-continental lithosphere. *Earth Planet. Sci. Lett.* **242**, 302–319 (2006).
34. Demouchy, S., Jacobsen, S. D., Gaillard, F. & Stern, C. R. Rapid magma ascent recorded by water diffusion profiles in mantle olivine. *Geology* **34**, 429–432 (2006).
35. Kelley, S. P. & Wartho, J. A. Rapid kimberlite ascent and the significance of Ar-Ar ages in xenolith phlogopites. *Science* **289**, 609–611 (2000).
36. Sparks, R. S. J., Pinkerton, H. & Macdonald, R. The transport of xenoliths in magmas. *Earth Planet. Sci. Lett.* **35**, 234–238 (1977).
37. O'Reilly, S. Y. & Griffin, W. L. Rates of magma ascent: constraints from mantle-derived xenoliths. *Timescales Magmat. Process. From Core Atmos.* **1803799613**, 116–124 (2010).
38. Anderson, O. L. The role of fracture dynamics in kimberlite pipe formation. *Kimberlites Diatremes Diamonds Their Geol. Petrol. Geochemistry* **15**, 344–353 (1982).
39. Lister, J. R. & Kerr, R. C. Fluid-mechanical models of crack propagation and their application to magma transport in dykes. *J. Geophys. Res. Solid Earth* **96**, 10049–10077 (1991).
40. Lensky, N. G., Niebo, R. W., Holloway, J. R., Lyakhovskiy, V. & Navon, O. Bubble nucleation as a trigger for xenolith entrapment in mantle melts. *Earth Planet. Sci. Lett.* **245**, 278–288 (2006).
41. Wilson, L. & Head, J. W. An integrated model of kimberlite ascent and eruption. *Nature* **447**, 53–57 (2007).
42. Brett, R. C., Russell, J. K., Andrews, G. D. M. & Jones, T. J. The ascent of kimberlite: Insights from olivine. *Earth Planet. Sci. Lett.* **424**, 119–131 (2015).
43. Kavanagh, J. L. & Sparks, R. S. J. Temperature changes in ascending kimberlite magma. *Earth Planet. Sci. Lett.* **286**, 404–413 (2009).
44. Iacovino, K. & Till, C. B. DensityX: a program for calculating the densities of magmatic liquids up to 1,627 C and 30 kbar. *Volcanica* **2**, 1–10 (2019).
45. Sparks, R. S. J. et al. Dynamical constraints on kimberlite volcanism. *J. Volcanol. Geotherm. Res.* **155**, 18–48 (2006).
46. Kirby, S. H. & Green, H. W. Dunite xenoliths from Hualalai volcano: evidence for mantle diapiric flow beneath the island of Hawaii. *Am. J. Sci.* **280**, 550–575 (1980).
47. Rudnick, R. L., Gao, S., Ling, W., Liu, Y. & McDonough, W. F. Petrology and geochemistry of spinel peridotite xenoliths from Hannuoba and Qixia, North China craton. *Lithos* **77**, 609–637 (2004).
48. Song, Y. & Frey, F. A. Geochemistry of peridotite xenoliths in basalt from Hannuoba, eastern China: implications for subcontinental mantle heterogeneity. *Geochim. Cosmochim. Acta* **53**, 97–113 (1989).
49. Carracedo, J. C., Rodriguez Badiola, E. & Soler, V. The 1730–1736 eruption of Lanzarote, Canary Islands: a long, high-magnitude basaltic fissure eruption. *J. Volcanol. Geotherm. Res.* **53**, 239–250 (1992).
50. Clague, D. A. Hawaiian xenolith populations, magma supply rates, and development of magma chambers. *Bull. Volcanol.* **49**, 577–587 (1987).
51. Kauahikaua, J., Cashman, K., Clague, D., Champion, D. & Hagstrum, J. Emplacement of the most recent lava flows on Hualalai Volcano, Hawai'i. *Bull. Volcanol.* **64**, 229–253 (2002).
52. Jankovics, M. É. et al. Origin and ascent history of unusually crystal-rich alkaline basaltic magmas from the western Pannonian Basin. *Bull. Volcanol.* **75**, 749 (2013).
53. Mattsson, H. B. Rapid magma ascent and short eruption durations in the Lake Natron-Engaruka monogenetic volcanic field (Tanzania): a case study of the olivine melilititic Pello Hill scoria cone. *J. Volcanol. Geotherm. Res.* **247**, 16–25 (2012).
54. McGetchin, T. R. & Ullrich, G. W. Xenoliths in maars and diatremes with inferences for the Moon, Mars, and Venus. *J. Geophys. Res.* **78**, 1833–1853 (1973).
55. Klügel, A., Schmincke, H.-U., White, J. D. L. & Hoernle, K. A. Chronology and volcanology of the 1949 multi-vent rift-zone eruption on La Palma (Canary Islands). *J. Volcanol. Geotherm. Res.* **94**, 267–282 (1999).
56. Ryerson, F. J., Weed, H. C. & Piwinski, A. J. Rheology of subliquidus magmas: 1. Picritic compositions. *J. Geophys. Res. Solid Earth* **93**, 3421–3436 (1988).
57. Vona, A. et al. Ascent velocity and dynamics of the Fiumicino mud eruption, Rome, Italy. *Geophys. Res. Lett.* **42**, 6244–6252 (2015).
58. Manga, M. & Bonini, M. Large historical eruptions at subaerial mud volcanoes, Italy. *Nat. Hazards Earth Syst. Sci.* **12**, 3377–3386 (2012).
59. Beris, A. N., Tsamopoulos, J. A., Armstrong, R. C. & Brown, R. A. Creeping motion of a sphere through a Bingham plastic. *J. Fluid Mech.* **158**, 219–244 (1985).
60. Tabuteau, H., Coussot, P. & de Bruyn, J. R. Drag force on a sphere in steady motion through a yield-stress fluid. *J. Rheol.* **51**, 125–137 (2007).
61. Mueller, S., Llewellyn, E. W. & Mader, H. M. The rheology of suspensions of solid particles. *Proc. R. Soc. A Math. Phys. Eng. Sci.* **466**, 1201–1228 (2010).
62. Heymann, L., Peukert, S. & Aksel, N. On the solid-liquid transition of concentrated suspensions in transient shear flow. *Rheol. Acta* **41**, 307–315 (2002).
63. Burchardt, S., Troll, V. R., Schmelting, H., Koyi, H. & Blythe, L. Erupted frothy xenoliths may explain lack of country-rock fragments in plutons. *Sci. Rep.* **6**, 34566 (2016).
64. Arndt, N. T. et al. Olivine, and the origin of kimberlite. *J. Petrol.* **51**, 573–602 (2010).
65. Arndt, N. T., Boullier, A.-M., Clément, J.-P., Dubois, M. & Schissel, D. What olivine, the neglected mineral, tells us about kimberlite petrogenesis. *eEarth Discuss* **1**, 37–50 (2006).
66. Sasse, D., Jones, T. J. & Russell, J. K. Transport, survival and modification of xenoliths and xenocrysts from source to surface. *Earth Planet. Sci. Lett.* **548**, 116499 (2020).
67. Jones, T. J., Russell, J. K. & Sasse, D. Modification of mantle cargo by turbulent ascent of kimberlite. *Front. Earth Sci.* **7**, 134 (2019).
68. Jones, T. J., Russell, J. K., Porritt, L. A. & Brown, R. J. Morphology and surface features of olivine in kimberlite: implications for ascent processes. *Solid Earth* **5**, 313 (2014).
69. Jones, T. J. & Russell, J. K. Attrition in the kimberlite system. *Mineral. Petrol.* **112**, 491–501 (2018).
70. Sachs, P. M. & Stange, S. Fast assimilation of xenoliths in magmas. *J. Geophys. Res. Solid Earth* **98**, 19741–19754 (1993).
71. Edwards, B. R. & Russell, J. K. Time scales of magmatic processes: new insights from dynamic models for magmatic assimilation. *Geology* **26**, 1103–1106 (1998).
72. Sparks, R. S. J. Kimberlite volcanism. *Annu. Rev. Earth Planet. Sci.* **41**, 497–528 (2013).
73. Shea, T. Bubble nucleation in magmas: a dominantly heterogeneous process? *J. Volcanol. Geotherm. Res.* **343**, 155–170 (2017).
74. Coffey, T. S. Diet Coke and Mentos: what is really behind this physical reaction? *Am. J. Phys.* **76**, 551–557 (2008).
75. Edwards, B. R. & Russell, J. K. Xenoliths as magmatic 'mentos' in AGU Spring Meeting Abstracts, EOS Transactions V22A-06 (2009).
76. Russell, J. K., Porritt, L. A., Lavallée, Y. & Dingwell, D. B. Kimberlite ascent by assimilation-fuelled buoyancy. *Nature* **481**, 352–356 (2012).
77. Vergnolle, S. & Jaupart, C. Separated two-phase flow and basaltic eruptions. *J. Geophys. Res. Solid Earth* **91**, 12842–12860 (1986).
78. Boyd, F. R. High- and low-temperature garnet peridotite xenoliths and their possible relation to the lithosphere-asthenosphere boundary beneath southern Africa. In *Mantle xenoliths* (ed. Nixon, P. H.) 403–412 (New York: John Wiley, 1987).
79. Mitchell, R. H. *Kimberlites: Petrology, Mineralogy and Geochemistry* (Springer Science & Business Media, 1986).
80. Shaikh, A. M., Tappe, S., Bussweiler, Y., Vollmer, C. & Brown, R. J. Origins of olivine in Earth's youngest kimberlite: Igwisi Hills volcanoes, Tanzania craton. *Contrib. to Mineral. Petrol.* **176**, 1–19 (2021).
81. Boyd, F. R. & Nixon, P. H. Origins of the ultramafic nodules from some kimberlites of northern Lesotho and the Monastery Mine, South Africa. *Physics and Chemistry of the Earth* **9** 431–454 (1975).
82. Tappe, S., Dongre, A., Liu, C.-Z. & Wu, F.-Y. 'Premier' evidence for prolonged kimberlite pipe formation and its influence on diamond transport from deep Earth. *Geology* **46**, 843–846 (2018).
83. Tappe, S., Smart, K., Torsvik, T., Massuyeau, M. & de Wit, M. Geodynamics of kimberlites on a cooling Earth: clues to plate tectonic evolution and deep volatile cycles. *Earth Planet. Sci. Lett.* **484**, 1–14 (2018).
84. Brown, R. J. et al. Eruption of kimberlite magmas: physical volcanology, geomorphology and age of the youngest kimberlitic volcanoes known on earth (the Upper Pleistocene/Holocene Igwisi Hills volcanoes, Tanzania). *Bull. Volcanol.* **74**, 1621–1643 (2012).

85. Dawson, J. B. Quaternary kimberlitic volcanism on the Tanzania Craton. *Contrib. Mineral. Petrol.* **116**, 473–485 (1994).
86. Porritt, L. A., Russell, J. K., McLean, H., Fomradas, G. & Eichenberg, D. A phreatomagmatic kimberlite: the A418 kimberlite pipe, Northwest Territories, Canada. In *Proceedings of 10th International Kimberlite Conference, Journal of the Geological Society of India*, Special issue Vol. 2 (eds Pearson, D. G. et al.) 97–107 (Springer, New Delhi, 2013).
87. Brown, R. J. & Valentine, G. A. Physical characteristics of kimberlite and basaltic intraplate volcanism and implications of a biased kimberlite record. *GSA Bull.* **125**, 1224–1238 (2013).
88. Peterson, N. D. *Carbonated Mantle Lithosphere in the Western Canadian Cordillera* (University of British Columbia, 2010).

Acknowledgements

J.K.R. was supported by the Natural Sciences and Engineering Research Council of Canada through the Discovery Grants program. T.J.J. was supported by a UK Research and Innovation Future Leaders Fellowship (MR/W009781/1).

Author contributions

J.K.R. and T.J.J. developed the concept together and equally contributed to defining the scope of the manuscript, performing the model calculations, preparing the figures, and writing the manuscript.

Competing interests

The authors declare no competing interests.

Additional information

Supplementary information The online version contains supplementary material available at <https://doi.org/10.1038/s43247-023-00843-0>.

Correspondence and requests for materials should be addressed to Thomas J. Jones.

Peer review information *Communications Earth & Environment* thanks John Faithfull, Michel Grégoire and Sebastian Tappe for their contribution to the peer review of this work. Primary Handling Editor: Joe Aslin. Peer reviewer reports are available.

Reprints and permission information is available at <http://www.nature.com/reprints>

Publisher's note Springer Nature remains neutral with regard to jurisdictional claims in published maps and institutional affiliations.



Open Access This article is licensed under a Creative Commons Attribution 4.0 International License, which permits use, sharing, adaptation, distribution and reproduction in any medium or format, as long as you give appropriate credit to the original author(s) and the source, provide a link to the Creative Commons license, and indicate if changes were made. The images or other third party material in this article are included in the article's Creative Commons license, unless indicated otherwise in a credit line to the material. If material is not included in the article's Creative Commons license and your intended use is not permitted by statutory regulation or exceeds the permitted use, you will need to obtain permission directly from the copyright holder. To view a copy of this license, visit <http://creativecommons.org/licenses/by/4.0/>.

© The Author(s) 2023